Chemical Science

ROYAL SOCIETY OF CHEMISTRY

EDGE ARTICLE

View Article Online
View Journal | View Issue

Cite this: *Chem. Sci.*, 2022, **13**, 3533

All publication charges for this article have been paid for by the Royal Society of Chemistry

π-Conjugated redox-active two-dimensional polymers as organic cathode materials†

Zexin Jin, ‡*[a] Qian Cheng, ‡[a] Austin M. Evans,[a] Jesse Gray,[a] Ruiwen Zhang,[b] Si Tong Bao,[a] Fengkai Wei,[b] Latha Venkataraman, [ab] Yuan Yang *[b] and Colin Nuckolls *[a]

Received 22nd December 2021
Accepted 2nd March 2022

DOI: 10.1039/d1sc07157b

rsc.li/chemical-science

Redox-active two-dimensional polymers (RA-2DPs) are promising lithium battery organic cathode materials due to their regular porosities and high chemical stabilities. However, weak electrical conductivities inherent to the non-conjugated molecular motifs used thus far limit device performance and the practical relevance of these materials. We herein address this problem by developing a modular approach to construct π-conjugated RA-2DPs with a new polycyclic aromatic redox-active building block **PDI-DA**. Efficient imine-condensation between **PDI-DA** and two polyfunctional amine nodes followed by quantitative alkyl chain removal produced RA-2DPs **TAPPy-PDI** and **TAPB-PDI** as conjugated, porous, polycrystalline networks. In-plane conjugation and permanent porosity endow these materials with high electrical conductivity and high ion diffusion rates. As such, both RA-2DPs function as organic cathode materials with good rate performance and excellent cycling stability. Importantly, the improved design enables higher areal mass-loadings than were previously available, which drives a practical demonstration of **TAPPy-PDI** as the power source for a series of LED lights. Collectively, this investigation discloses viable synthetic methodologies and design principles for the realization of high-performance organic cathode materials.

Introduction

Organic energy storage materials offer the prospect of high gravimetric energy storage with rapid charging and discharging rates without the need for costly, energy intensive and destructive resource acquisition.[1–3] Redox-active two-dimensional polymers (RA-2DPs, also referred to as covalent organic frameworks[4,5]) are among the most promising candidates as faradaic charge storage materials because of their tailored topologies and resultant regular porosities.[6–12] However, RA-2DPs have not reached their potential because the typical structures exhibit poor electrical conductivity[13,14] and their electro-inactive solubilizing moieties reduce the gravimetric energy storage performance.[15] This realization has led researchers to explore incorporating conducting additives[16–18] and exfoliating 2DPs into the few-layer limit[19] with the goal of increasing electrochemical accessibility. While these investigations demonstrate that increased electrochemical accessibility can improve faradaic performance in RA-2DPs, these strategies require laborious post-processing, expensive substrates and valuable additives. More importantly, the mass-loading of active materials in those devices is generally low[9] due to poor intrinsic electrical conductivity, which limits their deployment in practical devices.

In this study, we systematically examine the molecular design principles to improve faradaic charge storage in RA-2DPs. Specifically, we engineer a new redox-active motif: perylene diimide dibenzoaldehyde (**PDI-DA**, Fig. 1). PDI subunits can reversibly accept two electrons and have been widely used as acceptor materials for photovoltaics,[20] photodetectors,[21] redox flow batteries[22] and pseudocapacitors.[23] Conventionally, diimide-containing RA-2DPs are mostly extended through the imide nitrogen,[24] resulting in non-conjugated structures with limited electrical conductivity. Furthermore, these RA-2DPs frequently incorporate contorted phenyl spacers that diminish in-plane conjugation.[15,25] The **PDI-DA** unit studied here is bay connected through a fused aromatic ring that simultaneously addresses both limitations of previous molecular designs. To demonstrate the generality of these findings, we study two RA-2DPs prepared from different polyfunctional amine nodes: 1,3,6,8-tetrakis(4-aminophenyl)pyrene (**TAPPy**) and 1,3,5-tris(4-aminophenyl)benzene (**TAPB**). Following polymerization into crystalline, porous networks, the solubilizing alkyl side chains are quantitatively removed *via* thermolysis without disrupting the periodic network structures. This chemical transformation

[a]*Department of Chemistry, Columbia University, New York, New York 10027, USA. E-mail: zj2286@columbia.edu; cn37@columbia.edu*

[b]*Department of Applied Physics and Applied Mathematics, Columbia University, New York, New York 10027, USA. E-mail: yy2664@columbia.edu*

† Electronic supplementary information (ESI) available. See DOI: 10.1039/d1sc07157b

‡ These authors contributed equally to this work.

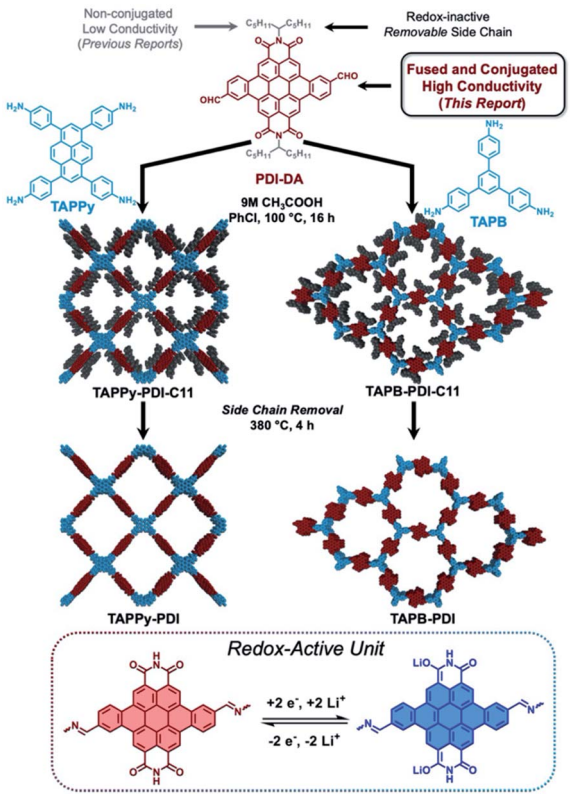

Fig. 1 Structure design of redox-active conjugated building blocks PDI-DA (top), synthesis of TAPPy-PDI (left) and TAPB-PDI (right) and depiction of their redox activity (bottom).

improves battery performance by decreasing the electrochemically non-participating mass and enhancing the lithium-ion permeability of the networks. As a result, RA-2DPs produced using the design principles uncovered here approach their theoretical capacity with excellent cycling stability.

Results and discussion

Synthesis of RA-2DPs

Fig. 1 displays the synthesis of RA-2DPs. Details for the synthesis of **PDI-DA** can be found in the ESI (Section 2†). RA-2DPs **TAPPy-PDI-C11** and **TAPB-PDI-C11** were then synthesized by acid catalyzed imine-condensation between **PDI-DA** and the corresponding polyamines. Both RA-2DPs were isolated in high yield (>90%) as crystalline, high surface area powders (*vide infra*). While performing thermogravimetric analysis (TGA) of these two polymers, we observed a ~30% sample mass loss for both 2DPs at ~380 °C (Fig. S1†). Previously, we have attributed this mass loss to thermal removal of the solubilizing side chains.[26] As such, alkyl chains were removed by heating at 380 °C under vacuum for 4 hours to yield **TAPPy-PDI** and **TAPB-PDI**, without disrupting the 2DP structures or imine-polymerization chemistry as determined by elemental analysis, infrared spectroscopy (see ESI†), X-ray diffraction, and nitrogen porosimetry.

Characterization of RA-2DPs

Fourier-transform infrared (FT-IR) spectroscopy shows that imine-condensation proceeded efficiently with high consumption of monomer functionality and thermolytic cleavage of the alkyl chains did not damage other chemical motifs within the networks. To better understand our FT-IR results, we prepared an imine-linked PDI-containing model compound (S4) by condensing **PDI-DA** with aniline under the same reaction conditions. Following imine condensation, the C=O stretch (1688 cm^{-1}) of the aldehyde and the N–H vibrational feature (3200 cm^{-1}) of the amine were found to disappear in both RA-2DPs and the model compound S4 (Fig. S2†). The imine C=N stretch (~1620 cm^{-1}) and the imide C=O stretch (~1607 cm^{-1}) are observed to overlap, which prevents definitive observation of the appearance of the expected polymerization chemistry.[15] Collectively, the FT-IR changes observed following polymerization confirm the imine-condensation product of aniline and **PDI-DA**. Thermolytic alkyl chain removal was verified by the disappearance of the alkyl vibrational modes (2800–3000 cm^{-1}) and concomitant increase of the N–H peak (3200 cm^{-1}). Importantly, the features associated with imide and imine moieties are found to be unaffected by the thermolysis procedure. This is consistent with the finding that the mass retention following thermolysis (70%) agrees well with the calculated mass retention of losing the side chains (73%). The FT-IR features observed throughout these chemical transformations correlate well with calculated vibrational spectra for each of these species (Fig. S3†).

Powder X-ray diffraction (PXRD) reveals that the **TAPPy-PDI-C11** and **TAPB-PDI-C11** and their thermolysis products were all isolated as polycrystalline powders (Fig. 2A). For both **TAPPy-PDI-C11** and **TAPB-PDI-C11**, sharp diffraction features were observed at low two theta values. We assigned these features as the ⟨100⟩ Bragg scattering features of a layered tetragonal and hexagonal network for **TAPPy-PDI-C11** and **TAPB-PDI-C11**, respectively. For both networks we also observed a diffuse scattering feature at high two theta values that we assign to the interlayer spacing between 2DP sheets in the solid-state. For **TAPPy-PDI-C11**, we find that the experimental pattern matches well with a simulated *C*2/*m* framework with lattice parameters of $a = b = 44.0$ Å, $c = 2.8$ Å with sharp diffraction features at 2.9°, 3.9° and 5.6° that correspond to the ⟨100⟩, ⟨200⟩ and ⟨220⟩ Bragg direction, respectively. For **TAPB-PDI-C11**, a simulated *P*6 framework is well matched with lattice parameters of $a = b =$ 46.8 Å, $c = 3.5$ Å with sharp diffraction features at 2.9°, and 4.4° that correspond to the reflections along the ⟨100⟩ and ⟨200⟩ planes. In both cases, the observed distances match well with the expected distances of the spatial distribution between the nodes. Following thermolysis both RA-2DPs exhibited practically unchanged diffraction patterns, which demonstrates that the structurally regular 2DP network is unperturbed after the side chain removal. All the experimental PXRD patterns were refined with finite crystal size broadening that revealed an average crystallite size >50 nm, consistent with other reports of high-quality polycrystalline 2DP powders.[27] These results are consistent with direct imaging *via* scanning electron

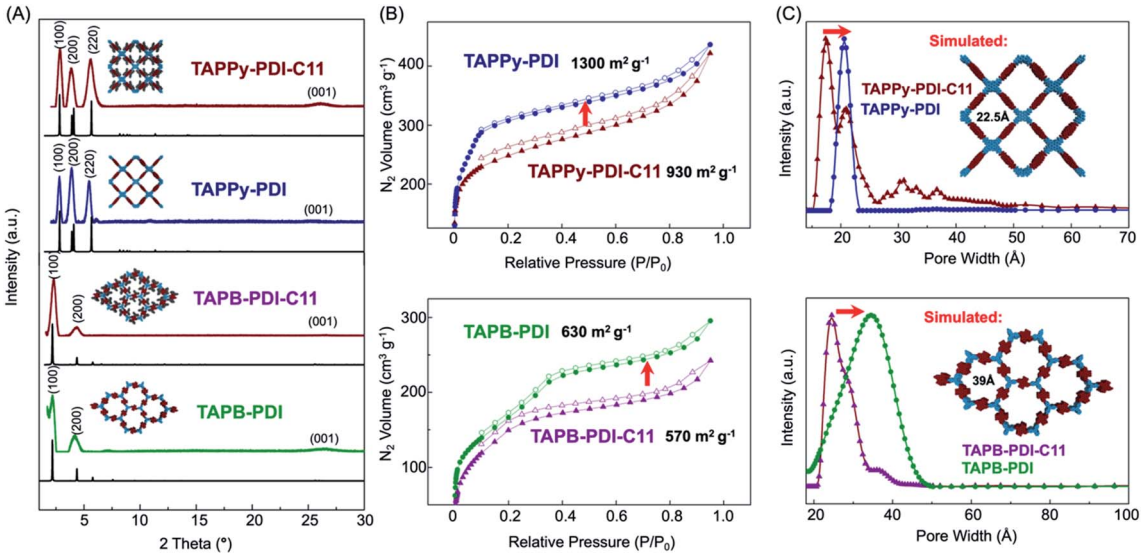

Fig. 2 (A) Background subtracted experimental (colored) and predicted (black) PXRD patterns, (B) nitrogen adsorption isotherms and (C) pore size distribution of RA-2DPs.

microscope showing that RA-2DPs are isolated as polycrystalline powders (Fig. S5†).

Nitrogen sorption isotherms in Fig. 2B establish that all four RA-2DPs were porous polymer networks. High Brunauer–Emmett–Teller (BET) surface areas of 930 $m^2\ g^{-1}$ and 570 $m^2\ g^{-1}$ were extracted for **TAPPy-PDI-C11** and **TAPB-PDI-C11**, respectively. Pore size distributions (Fig. 2C) were centered at 17 Å for **TAPPy-PDI-C11** and 24 Å for **TAPB-PDI-C11**. We attributed the relatively broad distribution to the disordered packing of the alkyl chains in the 2DP structures. Following thermolysis to remove the alkyl side chains, the BET surface areas of **TAPPy-PDI** and **TAPB-PDI** were increased to 1300 $m^2\ g^{-1}$ and 630 $m^2\ g^{-1}$. Increases in the BET surface area were accompanied by narrowing and increasing pore size distributions from 17 Å to 21 Å for **TAPPy-PDI** and 24 Å to 35 Å for **TAPB-PDI**, which correlates well with the structures determined from PXRD. Taken together, these results reveal that the RA-2DPs, in all forms, are isolated as structurally regular, permanently porous networks.

Electrochemical performance

Using these four crystalline, porous RA-2DPs, we performed comparative electrochemical experiments with lithium metal half-cells. The working electrodes were fabricated by drop casting a slurry of 70 wt% RA-2DPs, 20 wt% carbon black (as conductive agent, see Fig. S15† for lower mass loadings of conductive additive) and 10 wt% polyvinylidene fluoride (PVDF; as binder) in *N*-methyl-2-pyrrolidone onto a carbon paper. We then assembled the cell using working electrodes and lithium metal in 2032 coin cells with 1 M $LiPF_6$ in diethyl carbonate (DEC)/ethylene carbonate (EC) (1 : 1 vol) electrolyte. Cyclic voltammetry (CV) was first conducted on four RA-2DP electrodes with a scan rate of 1 mV s^{-1} (Fig. 3A). All the RA-2DPs exhibited fully reversible peaks centered at 2.2–2.3 V *vs.* Li/Li^+, corresponding to the redox reaction from PDI subunits. Under the same scan rate, **TAPPy-PDI** and **TAPB-PDI** showed much higher current and slightly more positive redox potentials than **TAPPy-PDI-C11** and **TAPB-PDI-C11**. This enhanced electrochemical performance after alkyl chain removal is likely attributed to the reduction of electrochemically inactive components, the increase of electrical conductivity and lithium-ion diffusion within the network (*vide infra*). It is noteworthy that the alkyl chain removal protocol should be applicable to many other RA-2DPs with solubilizing side chains to improve their device performance.[15,25] Because the RA-2DPs without the alkyl chains exhibit much higher capacity, we focused on investigating the device performance of **TAPPy-PDI** and **TAPB-PDI**.

The rate performance of **TAPPy-PDI** and **TAPB-PDI** were evaluated under different discharge rates from 0.1 A g^{-1} to 5 A g^{-1} (Fig. 3B). **TAPPy-PDI** delivered an initial capacity of 61 mA h g^{-1} at 0.1 A g^{-1} (1.5C), corresponding to 96% of the theoretical capacity. **TAPB-PDI**, on the other hand, exhibited slightly lower capacity (56 mA h g^{-1}) at the same rate, corresponding to 83% of its theoretical capacity. Both polymers showed outstanding rate performance due to their conjugated and porous structures. Even with a high current density of 5 A g^{-1} (80C), **TAPPy-PDI** and **TAPB-PDI** still retained 55% and 44% of their theoretical capacity, respectively. Such retention rates are much higher than those of conventional lithium-ion cathode materials.[1] These results show that we are able to fully unlock all the redox functional groups and significantly improve the rate performance by constructing the fully π-conjugated and porous network structures (see Table S1† for comparison with other materials).

Beyond the excellent rate performance, both RA-2DPs also possessed high cycling stability (Fig. 3C). At 0.5 A g^{-1} (7.5C), **TAPPy-PDI** showed a capacity of 52 mA h g^{-1} and an exceptional capacity retention of 83% after 1000 cycles, with an average

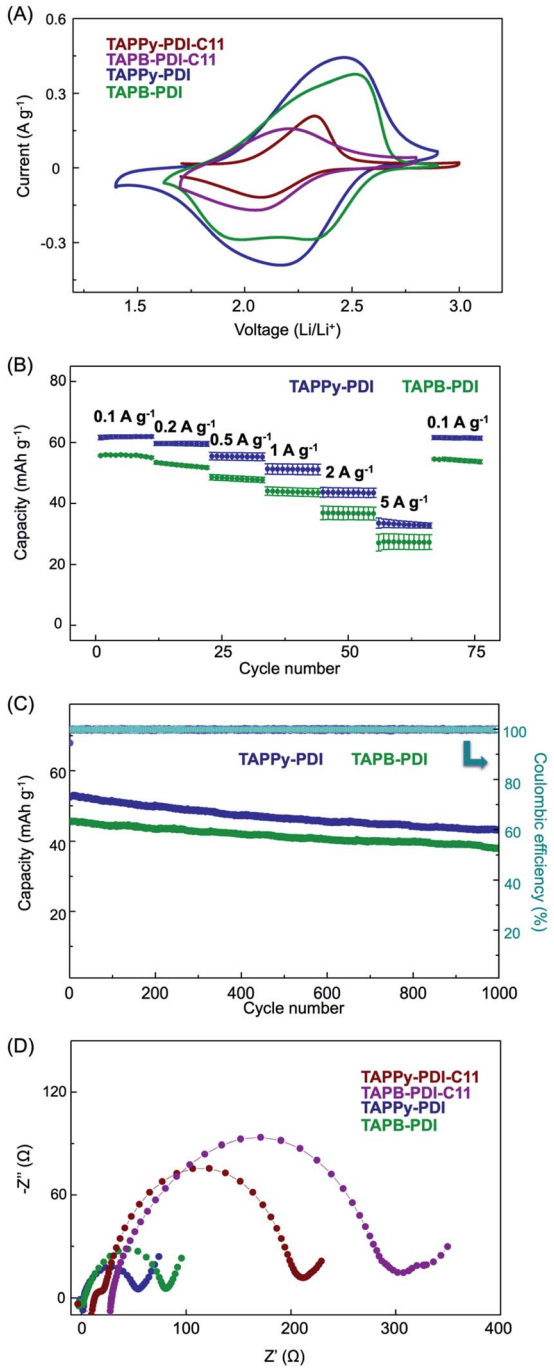

Fig. 3 The electrochemical performance of RA-2DPs. (A) CV profiles at 1 mV s^{-1} in 1.0 M $LiPF_6$ in DEC/EC (1 : 1 vol) electrolyte, (B) rate performance at different discharge rates, (C) cycling stability at 0.5 A g^{-1} and coulombic efficiency (TAPPy-PDI in purple circle and TAPB-PDI in cyan square) over 1000 cycles, and (D) EIS of RA-2DPs.

coulombic efficiency of 100%. **TAPB-PDI** exhibited a capacity of 45 mA h g^{-1} with 84% capacity retention after 1000 cycles at the same discharging rate. This superb cycling stability for both RA-2DPs can be attributed to the chemically and structurally robust two-dimensional networks.

To better understand the excellent device performance of **TAPPy-PDI** and **TAPB-PDI**, we performed electrochemical impedance spectroscopy (EIS) on all four 2DPs (Fig. 3D). The charge-transfer resistance (R_{ct}) of **TAPPy-PDI** and **TAPB-PDI** were determined as 57 Ω and 80 Ω, respectively, which are much lower than 2DPs with alkyl chains and those of similar polymer networks.[17] These low R_{ct} values of **TAPPy-PDI** and **TAPB-PDI** reveal high electrical conductivity (Table S2†) within the networks after alkyl chain removal, which may result from the full in-plane conjugation as well as the intimate π–π stacking of 2D sheets, as indicated by structural characterization data. To evaluate the lithium-ion diffusion within the networks, we analyzed the CV profiles at different scan rates for all four RA-2DPs. Using the Randles–Ševčík equation, the diffusion coefficient for **TAPPy-PDI**, **TAPB-PDI**, **TAPPy-PDI-C11** and **TAPB-PDI-C11** were determined to be 4.6×10^{-9} cm^2 s^{-1}, 3.6×10^{-9} cm^2 s^{-1}, 1.7×10^{-10} cm^2 s^{-1} and 4.7×10^{-11} cm^2 s^{-1}, respectively. These higher diffusion coefficients for both RA-2DPs without the alkyl chains likely result from the immense porosities of these networks, which facilitates lithium-ion diffusion. We attribute the better electrochemical performance of **TAPPy-PDI** than **TAPB-PDI** to the higher electrical conductivity and higher ionic diffusivity of **TAPPy-PDI**. Such high electrical conductivity and high lithium-ion diffusivity of **TAPPy-PDI** allows us to investigate the battery performance of cells with higher active material loading. As shown in Fig. S15,† **TAPPy-PDI** battery with >80% active material portion exhibited similar performance at charging rates below 10C. In addition, the cell with 80% active loading showed exceptional cycling stability, with a capacity retention of 83% after 1000 cycles at 0.5 A g^{-1} (Fig. S16†).

Necessity of the 2D crystalline structure

To demonstrate the necessity of the porous, two-dimensional and crystalline structure, we synthesized an amorphous **TAPPy-PDI** (**amp-TAPPy-PDI**) using ***cis*-PDI-DA** and **TAPPy** under the same protocol we developed (ESI, Section 4.3†). **Amp-TAPPy-PDI** exhibited no Bragg scattering and no BET surface area due to the amorphous structure. Despite the same chemical composition, **amp-TAPPy-PDI** exhibited much lower capacity (37 mA h g^{-1} at 0.1 A g^{-1}), rate performance (12 mA h g^{-1} at 0.5 A g^{-1}) compared to **TAPPy-PDI**. Correspondingly, the diffusion coefficient of **amp-TAPPy-PDI** was determined to be 1.2×10^{-10} cm^2 s^{-1}, which is an order of magnitude lower than of the structurally regular **TAPPy-PDI**. Therefore, we attribute the outstanding performance of **TAPPy-PDI** and **TAPB-PDI** to both high electrical conductivities resulting from the π-conjugated structures and the enhanced ion diffusion rates from the high porosity.

Practical demonstration

Given **TAPPy-PDI**'s superior device performance, we next evaluated it as high mass-loading charge storage media for practical applications. **TAPPy-PDI** was fabricated into electrodes with a mass-loading of ~5 mg cm^{-2}. Remarkably, the coin cells with high mass-loading electrodes still exhibited similar capacity (52 mA h g^{-1} at 0.2 A g^{-1}) to the lower mass-loading cells. We then used this coin cell battery to power up a light-emitting diode (LED) array to examine its power ability. As shown in

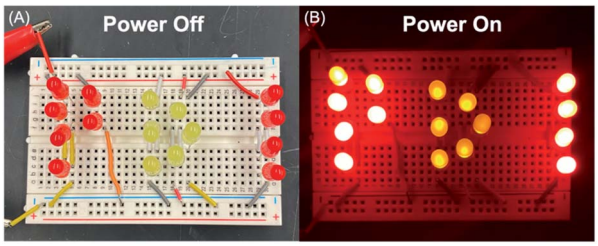

Fig. 4 Practical demonstration of TAPPy-PDI electrode coin cells: (A) power off and (B) power on status of the LED array.

Fig. 4A, the array was constructed with ten red LEDs and six orange LEDs. Using a potentiostat, the working currents of the red and orange LED bulbs were determined to be 0.1–0.2 mA. The forward voltage of red and orange LEDs was determined to be 2.0 V and 2.3 V respectively. Accordingly, the overall working current for the array is around 1.6–3.2 mA, corresponding to 5–10C of the battery. After being charged to 3 V at 5C, the battery was able to light up the array for 10 minutes (Fig. 4B and ESI video†). To note, the red LEDs were able to last even longer because of the lower required forward voltage. Therefore, we demonstrated the practical applications of these fully π-conjugated RA-2DPs by high mass-loading electrode coin cells.

Conclusions

To conclude, we have designed and synthesized new redox-active two-dimensional polymers by an efficient two-step approach with **PDI-DA** as the redox-active building block. All RA-2DPs were π-conjugated, polycrystalline and exhibited high porosity and high electrical conductivity. After alkyl chain removal, **TAPPy-PDI** and **TAPB-PDI** showed great potential as cathode materials in lithium batteries with good rate performance and excellent cycling stability. We attribute this to both high electrical conductivity and great ion diffusion rate, resulting from the in-plane conjugated and porous network structures. Finally, we demonstrated the practical applications of these new RA-2DPs by high mass-loading cells and using them to power up a LED array. Collectively, this study highlights the critical design principles and synthetic strategies to produce RA-2DPs as high-performance organic cathode materials.

Data availability

Detailed experimental procedures are included in the ESI.†

Author contributions

Conceptualization: Z. J., Q. C. and C. N.; methodology: Z. J. and Q. C.; investigation and formal analysis: Z. J., Q. C., A. M. E. and J. G.; validation: R. Z., S. T. B. and F. W.; writing – original draft: Z. J., Q. C. and A. M. E.; writing – review & editing: Y. Y. and C. N.; funding acquisition and supervision: L. V., Y. Y. and C. N.

Conflicts of interest

There are no conflicts to declare.

Acknowledgements

Primary support for this research was provided by the National Science Foundation under award DMR-2002634. The Columbia University Shared Materials Characterization Laboratory was used extensively for this research. We are grateful to Columbia University for support of this facility. C. N. thanks Sheldon and Dorothea Buckler for their generous support. A. M. E. is supported by the Schmidt Science Fellows, in partnership with the Rhodes Trust. We thank Dr Xiao Xiao and Dr Jingjing Yang for valuable discussions.

Notes and references

1 Y. Lu and J. Chen, *Nat. Rev. Chem.*, 2020, **4**, 127–142.
2 H. Lyu, X.-G. Sun and S. Dai, *Adv. Energy Sustain. Res.*, 2021, **2**, 2000044.
3 M. E. Bhosale, S. Chae, J. M. Kim and J. Y. Choi, *J. Mater. Chem. A*, 2018, **6**, 19885–19911.
4 N. W. Ockwig, A. P. Co, M. O. Keeffe, A. J. Matzger and O. M. Yaghi, *Science*, 2005, **310**, 1166–1171.
5 K. Geng, T. He, R. Liu, S. Dalapati, K. T. Tan, Z. Li, S. Tao, Y. Gong, Q. Jiang and D. Jiang, *Chem. Rev.*, 2020, **120**, 8814–8933.
6 A. M. Evans, M. J. Strauss, A. R. Corcos, Z. Hirani, W. Ji, L. S. Hamachi, X. Aguilar-Enriquez, A. D. Chavez, B. J. Smith and W. R. Dichtel, *Chem. Rev.*, 2022, **122**, 442–564.
7 C. S. Diercks and O. M. Yaghi, *Science*, 2017, **355**, eaal1585.
8 Y. Zhang, S. N. Riduan and J. Wang, *Chem.–Eur. J.*, 2017, **23**, 16419–16431.
9 V. Singh and H. R. Byon, *Mater. Adv.*, 2021, **2**, 3188–3212.
10 S. Kandambeth, V. S. Kale, O. Shekhah, H. N. Alshareef and M. Eddaoudi, *Adv. Energy Mater.*, 2021, 2100177.
11 Z. Meng, J. Luo, W. Li and K. A. Mirica, *J. Am. Chem. Soc.*, 2020, **142**, 21656–21669.
12 Z. Wang, S. Zhang, Y. Chen, Z. Zhang and S. Ma, *Chem. Soc. Rev.*, 2020, **49**, 708–735.
13 N. Huang, P. Wang and D. Jiang, *Nat. Rev. Mater.*, 2016, **1**, 16068.
14 Y. Jin, Y. Hu and W. Zhang, *Nat. Rev. Chem.*, 2017, **1**, 1–11.
15 S. Jhulki, C. H. Feriante, R. Mysyk, A. M. Evans, A. Magasinski, A. S. Raman, K. Turcheniuk, S. Barlow, W. R. Dichtel, G. Yushin and S. R. Marder, *ACS Appl. Energy Mater.*, 2021, **4**, 350–356.
16 C. R. Mulzer, L. Shen, R. P. Bisbey, J. R. McKone, N. Zhang, H. D. Abruña and W. R. Dichtel, *ACS Cent. Sci.*, 2016, **2**, 667–673.
17 E. Vitaku, C. N. Gannett, K. L. Carpenter, L. Shen, H. D. Abruña and W. R. Dichtel, *J. Am. Chem. Soc.*, 2020, **142**, 16–20.
18 F. Xu, S. Jin, H. Zhong, D. Wu, X. Yang, X. Chen, H. Wei, R. Fu and D. Jiang, *Sci. Rep.*, 2015, **5**, 1–6.

19 S. Wang, Q. Wang, P. Shao, Y. Han, X. Gao, L. Ma, S. Yuan, X. Ma, J. Zhou, X. Feng and B. Wang, *J. Am. Chem. Soc.*, 2017, **139**, 4258–4261.
20 Y. Zhong, M. T. Trinh, R. Chen, G. E. Purdum, P. P. Khlyabich, M. Sezen, S. Oh, H. Zhu, B. Fowler, B. Zhang, W. Wang, C. Y. Nam, M. Y. Sfeir, C. T. Black, M. L. Steigerwald, Y. L. Loo, F. Ng, X. Y. Zhu and C. Nuckolls, *Nat. Commun.*, 2015, **6**, 1–8.
21 Y. Zhong, T. J. Sisto, B. Zhang, K. Miyata, X.-Y. Zhu, M. L. Steigerwald, F. Ng and C. Nuckolls, *J. Am. Chem. Soc.*, 2017, **139**, 5644–5647.
22 M. Milton, Q. Cheng, Y. Yang, C. Nuckolls, R. Hernández Sánchez and T. J. Sisto, *Nano Lett.*, 2017, **17**, 7859–7863.
23 J. C. Russell, V. A. Posey, J. Gray, R. May, D. A. Reed, H. Zhang, L. E. Marbella, M. L. Steigerwald, Y. Yang, X. Roy, C. Nuckolls and S. R. Peurifoy, *Nat. Mater.*, 2021, **20**, 1136–1141.
24 S. Jin, K. Furukawa, M. Addicoat, L. Chen, S. Takahashi, S. Irle, T. Nakamura and D. Jiang, *Chem. Sci.*, 2013, **4**, 4505–4511.
25 Y. Liang, Z. Chen, Y. Jing, Y. Rong, A. Facchetti and Y. Yao, *J. Am. Chem. Soc.*, 2015, **137**, 4956–4959.
26 S. R. Peurifoy, J. C. Russell, T. J. Sisto, Y. Yang, X. Roy and C. Nuckolls, *J. Am. Chem. Soc.*, 2018, **140**, 10960–10964.
27 M. C. Daugherty, E. Vitaku, R. L. Li, A. M. Evans, A. D. Chavez and W. R. Dichtel, *Chem. Commun.*, 2019, **55**, 2680–2683.